Cryo-EM structure of the Smc5/6 holo-complex

Stephen T. Hallett[1], Isabella Campbell Harry[1],
Pascale Schellenberger[2], Lihong Zhou[1], Nora B. Cronin[3], Jonathan Baxter[1],
Thomas J. Etheridge[1*], Johanne M. Murray[1*] and Antony W. Oliver[1*]

1. Genome Damage and Stability Centre, School of Life Sciences, University of Sussex, Falmer, UK
2. Electron Microscopy Imaging Centre, School of Life Sciences, University of Sussex, Falmer, UK
3. London Consortium for CryoEM (LonCEM) Facility, The Francis Crick Institute, London, UK.

* To whom correspondence should be addressed:
TJE /// t.etheridge@sussex.ac.uk, ORCID: 0000-0001-8144-6917
JMM // j.m.murray@sussex.ac.uk, ORCID: 0000-0001-9225-6289
AWO // antony.oliver@sussex.ac.uk, ORCID: 0000-0002-2912-8273

ABSTRACT

The Smc5/6 complex plays an essential role in the resolution of recombination intermediates formed during mitosis or meiosis, or as a result of the cellular response to replication stress. It also functions as a restriction factor preventing viral integration. Here, we report the cryo-EM structure of the six-subunit budding yeast Smc5/6 holo-complex, reconstituted from recombinant proteins expressed in insect cells – providing a full overview of the complex in its apo / non-liganded form, and revealing how the Nse1/3/4 subcomplex binds to the hetero-dimeric SMC protein core. In addition, we demonstrate that a region within the head domain of Smc5, equivalent to the 'W-loop' of Smc4 or 'F-loop' of Smc1, mediates an essential interaction with Nse1. Taken together, these data confirm a degree of functional equivalence between the structurally unrelated KITE and HAWK accessory subunits associated with SMC complexes.

INTRODUCTION

The eukaryotic Structural Maintenance of Chromosomes (SMC) family includes the protein complexes cohesin, condensin and Smc5/6. At their respective 'hearts' sits an obligate heterodimer of two SMC proteins, either Smc1/Smc3, Smc2/Smc4 or Smc5/Smc6. Globular entities found at both the N- and C-termini of each SMC protein are brought together in space, to form a so-called 'head' domain that is capable of binding to, and turning over, ATP. The two halves of the ATPase are connected by a structural excursion known as the 'arm'; formed from sequential alpha-helical regions that coalesce to form a highly extended anti-parallel coiled-coil. The arm is interrupted at its apex (most distant point from the head) by the 'hinge' domain; a region of SMC proteins responsible for hetero-dimerisation with their obligate binding partner. The binding, hydrolysis, and release of ATP by the two head domains (one from each SMC protein) provides a secondary, more transient, and regulated dimerisation interface. The 'core' of each SMC complex is then elaborated through binding of additional 'non-SMC' protein subunits or 'elements', to provide the distinct functionalities required for their respective cellular functions.

For more expansive reviews of the SMC-family, including their respective functions and subunit compositions, please see: (Cutts and Vannini 2020; Datta, Lecomte, and Haering 2020; Hassler, Shaltiel, and Haering 2018; Matityahu and Onn 2021; Palecek 2018; Sole-Soler and Torres-Rosell 2020; Uhlmann 2016; Yatskevich, Rhodes, and Nasmyth 2019).

All three complexes are required for the organisation and management of chromosome architecture and structure throughout the cell cycle. Cohesin has well described roles in sister chromatid cohesion and the organisation of the interphase chromosomes into topologically associated domains or TADs, whereas condensin is required to compact chromosomes at mitosis. The Smc5/6 complex has roles in the processes of DNA replication and DNA damage repair; the complex acting to suppress / prevent formation of inappropriate structures that can form during homologous recombination-mediated rescue of replication forks that have stalled (or collapsed) on encountering replication 'road-blocks' or obstacles.

43 Alterations to the coding sequence of human Nse2 (Non-SMC-element; generally written as
44 either Nse or NSMCE) have been linked to primordial dwarfism and insulin resistance (Payne
45 et al. 2014), with changes in Nse3 linked to severe lung disease immunodeficiency and
46 chromosome breakage syndrome (LICS, (van der Crabben et al. 2016)). Interestingly, Smc5/6
47 is also specifically targeted for ubiquitylation and degradation by the regulatory protein X of
48 hepatitis B virus (HbX) to alleviate restriction of viral replication by the complex (Murphy et
49 al. 2016). The complex has also been shown to act as a restriction factor working against
50 other viruses (Bentley et al. 2018; Gibson and Androphy 2020; Xu et al. 2018).
51
52 As well as containing subunits that provide both ubiquitin and SUMO E3-ligase activity
53 (through Nse1 and Nse2 respectively), Smc5/6 is further differentiated from the cohesin and
54 condensin complexes by the fact that the two non-SMC proteins (Nse1 and Nse3) that bind
55 to its kleisin subunit (Nse4) belong to the 'KITE' family (kleisin-interacting tandem winged-
56 helix element; (Palecek and Gruber 2015)) rather than the distinct and structurally unrelated
57 'HAWK' family (HEAT proteins associated with kleisins; (Wells et al. 2017). As proteins of the
58 KITE-family are also found in prokaryotic SMC complexes, it has led to the hypothesis that
59 Smc5/6 best represents the eukaryotic 'cousin' of *Bacillus subtilis* Smc/ScpAB and *Escherichia*
60 *coli* MukBEF (Palecek and Gruber 2015) — however, it is still unclear as to when in the
61 evolutionary timescale KITEs were replaced by HAWK subunits, to create cohesin and
62 condensin complexes.
63
64 Here, we present the cryo-EM structure of the budding yeast Smc5/6 complex, in its apo or
65 non-liganded form. Our study serves to confirm the overall architecture of the complex, plus
66 provide details of how and where the Nse1/Nse3/Nse4 KITE-kleisin subcomplex interacts with
67 the Smc5/Smc6/Nse2 core. Additional experiments reveal the presence of a crucial interface
68 formed between the head domain of Smc5 and Nse1, which utilises the equivalent of the 'W-
69 loop' or 'F-loop' found in Smc4 and Smc1 respectively (Hassler et al. 2019). Taken together,
70 our data uncover an unanticipated degree of functional equivalence between KITE and HAWK
71 accessory subunits.

RESULTS

In this manuscript, for simplicity and brevity, we refer to the protein components of the *Saccharomyces cerevisiae* SMC complexes, unless otherwise indicated.

We have previously described reconstitution and characterisation of the *S. cerevisiae* Smc5/6 complex, using recombinant proteins expressed in insect cells (Hallett et al. 2021). Here, cryo-EM data were collected for the six component 'holo-complex', where Smc5 and Smc6 contain Walker B mutations E1015Q and E1048Q, respectively (**Fig. 1a, Materials and Methods**).

A neural network was trained with a set of manually picked particles (Bepler et al. 2019). The resultant 'picking model' was then used to identify a total of 380,714 particles (see **Sup. Fig. 1** for data-processing summary). Two sets of two-dimensional (2D) class averages emerged from processed data, with either the 'hinge' (**Fig. 1b, top**) or the 'head-end' of the complex more clearly in focus (**Fig. 1b, bottom**); the blurred density at either end consistent with a degree of conformational flexibility within the coiled coil 'arms' (Hallett et al. 2021). From this, a sub-set of 17,162 particles were used to generate a medium-resolution 3-dimensional (3D) map that covered the entire length of the holo-complex, reconstructed at a resolution of 10.8 Å as judged by the 0.143 Fourier shell correlation (FCS) criterion (Rosenthal and Henderson 2003) (**Fig. 1c**). Focussed refinement allowed a slightly higher resolution map to be calculated for the upper (106,660 particles, 8.5 Å) segment of the complex (**Fig. 1d**). Pleasingly, resultant maps were consistent with the envelope we previously obtained by uranyl acetate negative stain transmission electron microscopy (Hallett et al. 2021), **Fig. 1d, inset**).

In parallel, we trained a second neural network with manually picked particles that encompassed just the head-end of the complex (824,644 particles). The resultant 2D class averages and 3D map from processed data (84,180 particles, 6.5 Å) are shown in **Fig. 1e** and **1f** respectively. Segmentation analysis (Pettersen et al. 2021; Pintilie and Chiu 2012; Pintilie et al. 2010) allowed portions of the map to be readily assigned to the head domains, as well as the Nse1/Nse3/Nse4 (Nse1/3/4) subcomplex (coloured red, blue and grey respectively in **Fig. 1f**). Additional segments of density associated with either the 'head' or 'arm' (dark or light

green, **Fig. 1f**) allowed the identity of each head-domain to be determined, due the expected binding positions of the N- and C-terminal domains of the kleisin Nse4 (please see additional text below).

A model for the Smc5/6 holo-complex

A sharpened composite map, generated from the highest resolution maps for each segment of the holo-complex, was of sufficient quality to allow positioning of the coiled-coil regions for both Smc5 and Smc6, as well as placement of the structure of *S. cerevisiae* Nse2 (Mms21) bound to the arm of Smc5 (PDB: 3HTX; (Duan et al. 2009). This, combined with homology models for the 'hinge', 'heads' and Nse1/3/4, allowed an initial pseudo-atomic model to be constructed; this model was subsequently updated using AlphaFold predictions made available through the EMBL-EBI repository (https://alphafold.ebi.ac.uk; (Jumper et al. 2021) (see **Materials and Methods**).

Working from the 'top' of the complex downwards, we see that the hinge domain is tilted with respect to an axis defined by the coiled-coil arms; consistent with our previous analysis of this region in the fission yeast complex and with data published for condensin (Alt et al. 2017; Soh et al. 2015). Below this, there is an apparent discontinuity / break in the helices of the arms, located between the hinge and Nse2 subunit — a feature likely to represent the 'elbow' found in the other complexes of the SMC-family (Burmann et al. 2019; Kong et al. 2020; Lee et al. 2020) — notably, at this point the two arms of Smc5/6 also cross over each other (**Fig. 2a**, inset *ii*).

In our previous lower-resolution study, we observed that the arms of Smc5/6 remain in close proximity ('arms-together', 'rod-like', 'I'-conformation) for the majority of their length (Hallett et al. 2021), in agreement with parallel studies published by other laboratories (Gutierrez-Escribano et al. 2020; Taschner et al. 2021; Yu et al. 2021). With the additional resolution now afforded by cryo-EM, we see that the arms separate slightly from each other after the junction with Nse2 (**Fig. 2a**, inset *iii*) but then remain approximately parallel until the head-end of the complex. Our model positions the first alpha-helix (α1) of Nse2 such that it can 'talk' across to the descending helix (hinge to head) of Smc6, as well as make its previously documented set of interactions with Smc5 (Duan et al. 2009); the helix appearing to 'glue'

135 the two arms together, in agreement with crosslinking data for the holo-complex recently
136 published by (Taschner et al. 2021) (**Sup. Fig. 2a**). The two arms then briefly re-contact each
137 other, through the two inward facing helices (αC3) of the 'joint' (**Fig. 2a,** inset *iv*) — a
138 molecular feature common to SMC proteins (Diebold-Durand et al. 2017) formed from three
139 helix-loop repeats that encircle the more continuous ascending alpha-helix, thus generating
140 both an interruption and point of flexure within the coiled-coiled structure of the arm; again
141 supported by crosslinking data (**Sup. Fig. 2b**; (Taschner et al. 2021)).
142
143 In our model, the head domains of Smc5 and Smc6 are not in direct contact. Comparison of
144 head domain positions indicates that our structure most resembles that of the apo / ATP-free
145 / 'non-engaged' / juxtaposed / or 'J'-state of budding yeast condensin deposited under PDB
146 accession code 6YVU (Lee et al. 2020) rather than the ATP-bound / 'engaged' / 'E'-state seen
147 for budding yeast cohesin when in complex with Scc2 and DNA (PDB: 6ZZ6; (Collier et al. 2020)
148 (**Fig. 2b**). Sections of the map corresponding to the RecA lobe of both the Smc5 and Smc6
149 head domain become less apparent at higher contour levels, suggesting a degree of
150 conformational flexibility in this part of the complex, as supported by estimates of local
151 resolution (**Sup. Fig. 2c**).
152
153 **Revealing the binding location of the Nse1/3/4 sub-complex**
154 The Nse1/3/4 subcomplex is located to one side of the central axis defined by the coiled-coil
155 arms of Smc5 and Smc6. The winged-helix 2 (WH/2) domain of Nse1 and the head domain of
156 Smc5 are in direct contact, with a short loop protruding from the equivalent winged-helix
157 domain of Nse3 (WH/B) positioned to interact with the arm of Smc5 (amino acids 244-254,
158 **Fig. 2a** inset *v*). Notably, neither Nse1 nor Nse3 directly interact with Smc6.
159
160 The recent publication of an X-ray crystal structure for *Xenopus laevis* Nse1/3/4, has provided
161 molecular details for how the kleisin subunit interacts with the Nse1/Nse3 KITE heterodimer
162 (kleisin-interacting tandem winged-helix element). The central section of Nse4 follows a path
163 through the centre of both KITE proteins, interacting with the linker regions that serve to
164 connect their component winged-helix domains together (Jo et al. 2021). Pleasingly, our cryo-
165 EM data allows integration of this kleisin path with the set of interactions made by the
166 globular domains found at each of its termini: the helical N-terminal domain binding to the

167 'neck' of Smc6 (**Fig. 1f and 2c**) and the C-terminal domain to the 'cap' of the Smc5 head
168 domain (**Fig. 1f and 2d**, **left**) thus confirming at the structural level the set of kleisin-facilitated
169 interactions conserved across the SMC-family of complexes, including prokaryotic ScpAB and
170 MukBEF as well as eukaryotic condensin and cohesin (Burmann et al. 2013; Diebold-Durand
171 et al. 2017; Fennell-Fezzie et al. 2005; Gligoris et al. 2014; Haering et al. 2004; Kamada et al.
172 2017; Woo et al. 2009; Zawadzka et al. 2018). Saying this, the resolution of our composite
173 map is not sufficient to allow an unambiguous tracing of the parts of Nse4 that serve to
174 connect the N-terminal domain to the central section (amino acids 125-183) or the central
175 section to the C-terminal domain (aa 46-283), indicating either intrinsic disorder or a high
176 degree of conformational flexibility; an observation consistent with the kleisin moieties in
177 cryo-EM structures of other eukaryotic SMC complexes (Collier et al. 2020; Higashi et al. 2020;
178 Lee et al. 2020; Shi et al. 2020).
179
180 **Additional structural features are predicted by AlphaFold**
181 AlphaFold predicts (albeit with a lower level of confidence) the presence of a hereto unknown
182 alpha-helical element in the C-terminal domain of Nse4 (amino acids Ser360 through to
183 Ala372). Nicely, this provides a facile explanation for a region of additional density visible in
184 our composite map, not accounted for by the initial homology model (**Fig. 2d left**). Similarly,
185 AlphaFold predicts the presence of a budding yeast-specific extended loop within the NH-
186 RING domain of Nse1 (amino acids Glu287 to Gln303), which again provides a better overall
187 fit to the experimental map (**Fig. 2d right, Supp. Fig 2d**).
188
189 **A loop in Smc5 has functional equivalence to the W-loop of Smc4 and F-loop of Smc1**
190 The location of Nse1/3/4 binding is particularly striking, as it echoes that of the structurally
191 unrelated HAWK accessory proteins (HEAT proteins associated with kleisins) found in
192 condensin and cohesin complexes; in each case, the head domain of the κ-SMC (Smc5, Smc4,
193 Smc1) serving to provide a major interaction surface (**Fig. 3a**).
194
195 Closer inspection reveals that a region of Smc5 (amino acids Gly947—Gly978), which 'talks'
196 across to the Nse1 subunit, is structurally equivalent to the 'W-loop' of the Smc4 head domain
197 (Hassler et al. 2019) (**Fig. 3b, 3c inset**). Notably, defined mutations (S1316D or W1317A)
198 introduced into the W-loop render budding yeast cells non-viable. Furthermore, in the

199 context of a fully recombinant 'head complex', mutation of the equivalent tryptophan residue
200 in *Chaetomium thermophilum* (*Ct*) Smc4 resulted in a dramatic reduction of its ability to
201 turnover ATP (Hassler et al. 2019). In Smc1, the equivalent region has been given the
202 alternative title of 'F-loop', due to the presence of a conserved phenylalanine residue (F1123
203 in budding yeast Smc1; (Hassler et al. 2019; Petela et al. 2021; Shi et al. 2020).
204
205 In Smc5, Leu978 appears to be the structurally equivalent 'F' or 'W-loop' residue (**Fig. 3b**) — a
206 relationship supported by a strong preference for a leucine in this position, as revealed by a
207 cross-species multiple amino acid sequence alignment (**Fig. 3c**). However, two additional
208 amino acids within the same loop, Phe972 and Leu981, are also strictly conserved (label F in
209 **Fig. 3b** and **c**). A second region of conservation was also evident in the preceding loop
210 (labelled Y in **Fig. 3b and c**). Here, structural comparison suggested that one or more aromatic
211 residues might potentially act to anchor or connect the helical lobe of the head domain back
212 to its coiled-coil arm. Interestingly, in *E. coli* MukB, this region is highly elaborated to form the
213 so-called 'larynx', residues of which contribute to its DNA-binding interface (Bürmann et al,
214 2021; https://doi.org/10.1101/2021.06.29.450292).
215
216 When working with homology models and structural data of limited resolution, there is a
217 degree of uncertainty as to the precise amino acids involved in a molecular interface. With
218 this in mind, we introduced sets of mutations designed to either disrupt localised structure
219 or alter key features within a loop (**Materials and Methods**). Yeast harbouring the (Y) Y961A,
220 W964A double mutation were viable and surprisingly displayed no sensitivity to a range of
221 genotoxic agents. In sharp contrast, introduction of the (F) F972A, L978D, L981N triple mutant
222 rendered budding yeast cell inviable, as determined by dissecting sporulated diploids (**Fig. 3c,**
223 **Sup. Fig. 3a**); confirming the importance of this loop to cellular function. We also introduced
224 a set of complementary mutations into Nse1, designed to perturb the interaction with the
225 Smc5 loop (N: F217A, E228R, R242A). Here, yeast were viable, but had a slow growth
226 phenotype and mild sensitivity to treatment with MMS or camptothecin (**Fig. 3c and Sup.**
227 **Figs. 3c and 3d**).

228 **DISCUSSION**

229 Using recombinant proteins expressed in insect cells we have reconstituted, then visualised
230 by cryo-EM, the six-subunit budding yeast Smc5/6 'holo-complex' — in its apo or unliganded
231 form — to provide a structural overview of the complex's architecture and reveal the position
232 of the bound Nse1/3/4 sub-complex. Whilst structurally unrelated to the HAWK-family of
233 proteins (HEAT proteins associated with kleisins; (Wells et al. 2017) the set and type of
234 interactions made by the KITE (kleisin-interacting tandem winged-helix element; (Palecek and
235 Gruber 2015) hetero-dimer of Nse1/3 and the kleisin Nse4 indicate several unifying features
236 that span the SMC-family of complexes:

237

238 *i) KITE and HAWK subunits can bind to double-stranded DNA*

239 **Smc5/6:** The ability of the Smc5/6 complex to bind dsDNA is provided by the Nse1/3
240 heterodimer (see also text below, (Zabrady et al. 2016). Furthermore, reconstituted
241 complexes lacking both Nse1/3 and the kleisin Nse4 do not bind dsDNA (Hallett et al. 2021).
242 In condensin and cohesin, a similar dsDNA-binding activity is provided by the HAWK subunits,
243 with the notable exception of Pds5 (Li et al. 2018). **Condensin:** Both the Brn1-Ycg1-Ycs4
244 hetero-trimer (Piazza et al. 2014) as well as Ycg1 in complex with the C-terminal portion of
245 Brn1 (Kschonsak et al. 2017) can interact with nucleic acid. Whilst DNA-binding by Ycs4 has
246 not been formally demonstrated, an examination of its structure and surface charge suggests
247 the presence of a compatible region located between HEAT repeats 7 and 8 (Lee et al. 2020);
248 a view supported by experiments using *Ct*Ycs4 and *Ct*Ycg1 which, as isolated proteins, have
249 affinity for dsDNA (Piazza et al. 2014). **Cohesin:** Scc3, when bound to Scc1, is capable of
250 binding to dsDNA (Li et al. 2018). DNA-binding has been reported for Mis4, the *S. pombe*
251 equivalent of Scc2, both in the context of its hetero-dimeric complex with Ssl3 (equivalent to
252 Scc4) or as an isolated protein (Murayama and Uhlmann 2014; Kurokawa and Murayama
253 2020). Recent data indicates a similar pattern of behaviour for both the Scc2/Scc4 hetero-
254 dimer and for Scc2 alone [Collier *et al.*, 2020; https://doi.org/10.1101/2020.06.03.132233].

255

256 *ii) Addition of dsDNA stimulates ATPase activity*

257 **Smc5/6**: Addition of dsDNA to Smc5/6 strongly stimulates its ATPase activity (Fousteri and
258 Lehmann 2000) with enhancement being strictly dependent on the presence of the Nse1/3/4

259 sub-complex (Hallett et al. 2021). **Condensin:** Similarly, the Brn1-Ycg1-Ycs4 or 'non-SMC'
260 complex is essential for dsDNA-dependent simulation of ATPase activity (Piazza et al. 2014).
261 **Cohesin:** Here, the Scc2 subunit is required, as determined by experiments that added the
262 protein to pre-assembled complexes containing either the core hetero-trimer
263 (Smc1/Smc3/Scc1) or hetero-tetramer (Smc1/Smc3/Scc1/Scc3) (Petela et al. 2018). A similar
264 requirement has been demonstrated for the fission yeast cohesin complex (Murayama and
265 Uhlmann 2014). In each case, the presence of the kleisin subunit is required to connect the
266 dsDNA binding activity of the KITE/HAWK protein to the core SMC complex.
267
268 *iii) dsDNA-binding is intrinsically linked to chromatin-binding, loading or retention*
269 **Smc5/6:** Hypomorphic (non-lethal) mutations that reduce the ability of the Smc5/6 complex
270 to bind to dsDNA, result in a loss of chromatin association, as shown by chromatin immuno-
271 precipitation (ChIP) and live-cell single-molecule tracking experiments (Etheridge et al. 2021;
272 Zabrady et al. 2016). **Condensin:** Mutations that reduce the ability of Brn1 to interact with
273 dsDNA, as part of its composite interaction surface with Ycg1, reduce the amount of
274 condensin associated with chromatin at defined loci (Kschonsak et al. 2017). **Cohesin:**
275 Mutations that affect the ability of Scc2 or Mis4 to bind DNA result in reduced chromatin
276 binding/loading, at several known cohesin-enriched loci (Collier et al. 2020; Kurokawa and
277 Murayama 2020).
278
279 *iv) mutations within the W-loop (or equivalent) of the κ-SMC perturb function*
280 The 'W-loop' is a conserved structural feature, present in each of the κ-SMC subunits (Smc1,
281 Smc4, Smc5) albeit with different patterns of amino acid conservation. Mutation of highly
282 conserved amino acids within the loop are incompatible with cell viability of yeast when
283 introduced into Smc4 (Hassler et al. 2019) or Smc5 (this manuscript).
284
285 By taking each of the above points in hand, we can now add the Nse1/3 hetero-dimer into
286 the statement made by (Petela et al. 2018) "A role in contacting DNA might therefore be a
287 feature conserved between Scc2 and Ycg1" and also amend the statement made by (Hassler
288 et al. 2019) that '…interaction of a HEAT-repeat subunit with the κ-SMC_{hd} (head domain) is a
289 central feature of all condensin and cohesin complexes' — to also include Smc5/6 — to state

290 that ‘interaction of a kleisin-associated subunit, whether HAWK or KITE, with the κ-SMC head
291 domain is a central feature of the hetero-dimeric SMC complexes, condensin, cohesin and
292 Smc5/6.’
293
294 **A speculative model for DNA-binding and engagement**
295 (Zabrady et al. 2016) previously reported a docking pose for binding of a double-stranded
296 DNA duplex to a positively charged cleft formed between human Nse1 and Nse3
297 (NSMCE1/NSMCE3) supported by a range of biochemical and biophysical data. A more recent
298 study using *Xenopus laevis* Nse1/3/4 has reported a similar mode of interaction (Jo et al.
299 2021). By simple superposition, one end of the docked DNA duplex would physically clash
300 with the arm of Smc5 (**Fig. 4a, left**). However, the DNA duplex could be accommodated by a
301 relatively small movement of the Nse1/3/4 subcomplex away from the Smc5 head domain
302 (or vice versa). Saying this, the resulting pose would still be at odds with the expected dsDNA
303 binding location, as illustrated here by comparison to the DNA-bound *S. cerevisiae* cohesin
304 complex (**Fig. 4a, right**. SMC1-SMC3-SCC1-SCC2 complex; PDB: 6ZZ6), but also observed for
305 other proteins of the SMC-family, including the more distantly related Rad50 (Kashammer et
306 al. 2019).
307
308 In their 2019 paper, Hassler et al. state that ‘It is likely that tilting and repositioning of the W-
309 loop residues dissociates Ycs4, which binds this part of $Smc4_{hd}$ (head-domain) and sterically
310 blocks access of $Smc2_{hd}$’. The follow-on study builds on this initial hypothesis to uncover a
311 ‘flip-flop’ mechanism, which involves a physical switch of HEAT subunit from Ycs4 (binding to
312 the head domain of Smc4) in the apo/unliganded state, to Ycs1 (binding to the head domain
313 of Smc2) in the engaged/ATP-bound state (Lee et al. 2020). It is therefore tempting to
314 speculate that a similar mechanism may well be at play in Smc5/6, as in order for the head-
315 domain of Smc5 to become engaged with that of Smc6, a conformational change is dictated
316 — potentially linked to breaking of the Smc5 ‘W-loop’ / Nse1 interface, to release and allow
317 repositioning of the KITE sub-complex, and thus facilitate engagement of a bound dsDNA
318 substrate with the top section of each head domain (see speculative model presented in **Fig.**
319 **4b**). Here, however, a ‘flip-flop’ mechanism might invoke the Nse3 subunit and a potential
320 direct interaction with the head domain of Smc6. This will, however, require experimental
321 validation, especially given that in PDB entry 6ZZ6 (cohesin) the F-loop of Smc1 remains

322 engaged with the Scc2 subunit, indicating that the precise molecular choreography
323 underpinning the initial 'engagement' complex is still unclear, and may well be (subtly?)
324 different for each complex of the SMC-family in accordance with their respective cellular
325 functions.
326
327 **Does Nse2 prevent or control bending at the elbow?**
328 We and others have observed some degree of flexure at the 'elbow' of Smc5/6 (Gutierrez-
329 Escribano et al. 2020; Hallett et al. 2021; Serrano et al. 2020; Taschner et al. 2021; Yu et al.
330 2021) but without the acute bend observed in condensin, cohesin and MukBEF (Anderson et
331 al. 2002; Burmann et al. 2019; Collier et al. 2020; Higashi et al. 2020; Kong et al. 2020; Lee et
332 al. 2020; Shi et al. 2020). However, the set of interactions made by Nse2 with Smc5, and now
333 Smc6, may provide insight, as these are likely to prevent separation and rotation of the arms,
334 and therefore the concerted set of motions thought to produce the bend (Burmann et al.,
335 2019).
336
337 Interestingly, a major hotspot for auto-SUMOylation has been mapped to a region within the
338 coiled-coil arm of Smc5, sitting between amino acids Lys310 and Lys327. Whilst the precise
339 site(s) of modification appears to be redundant, Lys311 has been identified with high
340 confidence as a major site of auto-SUMOylation (Zapatka et al. 2019). Saying this, it is not
341 known what effect SUMOylation has on the overall structure / conformation of the Smc5/6
342 holo-complex, but the proximity of the primary modification site to the α1-helix of Nse2 hints
343 at a regulatory role; potentially one that acts to control arm 'architecture' (**Fig. 2**, inset *iii*) as
344 well as performing the documented roles in promoting interactions with, and / or modulating
345 activity of, replication fork associated-DNA helicases such as Sgs1^{BLM} (Bermudez-Lopez et al.
346 2016) and Mph1^{FANCM} (Xue et al. 2014).
347
348 Interestingly, SUMOylation catalysed by the Smc5/6 complex has been shown to be
349 stimulated by the addition of single-stranded DNA (ssDNA) to reaction mixes (Varejao et al.
350 2018) with circular dichroism experiments showing localised changes in the secondary
351 structure of Smc5 upon DNA-engagement. We speculate that this is likely to occur as a direct
352 consequence of an initial binding event at the hinge-region of the complex, that leads to
353 stimulation and auto-modification of Smc5/6, which then allows the complex to

354 control/modulate homologous recombination activity at a stalled replication fork,
355 presumably through regulation of specific helicases and/or other modified substrates;
356 supported by our experimental observations in fission yeast, where mutations affecting the
357 ability of the hinge to bind ssDNA lead to gross chromosomal rearrangements, but do not
358 impact chromatin-binding or retention of the complex {Etheridge, 2021 #164}.
359
360 Finally, our cryo-EM structure of the apo/non-liganded state provides a highly valuable
361 'stepping stone' along the way to a fuller understanding of the set of molecular interactions
362 and dynamics than underpin the cellular function(s) of the Smc5/6 complex. Clearly, a
363 desirable goal is now the determination of structures for the ATP-bound and DNA-engaged
364 states.

365 ## MATERIAL AND METHODS

366 **Expression and purification**

367 Detailed experimental procedures for both expression and purification of the *S. cerevisiae*
368 Smc5/6 holo-complex are available in (Hallett et al. 2021). For convenience, the composition
369 of the two buffers that have been used in this study are listed below:

370 **BUFFER C:** 20 mM HEPES.NaOH pH 7.5, 100 mM NaCl, 0.5 mM TCEP

371 **BUFFER F:** 20 mM HEPES.NaOH pH 7.5, 0.5 mM TCEP

372

373 **Cryo-EM**

374 ***Sample preparation***

375 Fractions eluting from a Superose 6 size exclusion chromatography column (equilibrated in
376 BUFFER C; Cytiva Life Sciences, Little Chalfont, UK), corresponding to BS3-crosslinked holo-
377 complex, were immediately used for grid preparation. The sample was diluted by a factor of
378 two (with addition of BUFFER F) to reduce the overall NaCl concentration to 50 mM and yield
379 a final concentration of 0.1 mg/ml. From this, 3 μl was applied to a freshly glow-discharged
380 grid (Quantifoil R0.6/1 Cu 300 mesh grid; 60 seconds, 15 mA, PELCO easiGlow — Agar
381 Scientific, Stansted, UK). Using an EM GP2 automatic plunge freezer (Leica Microsystems,
382 Wetzlar, Germany) the grid was held in a chamber at 10 °C and 90% relative humidity, for a
383 period of 10 seconds, before blotting for 2.5 - 4.5 seconds using the auto-sensor. The grid was
384 immediately plunged into liquid ethane at -182 ° and then stored under liquid nitrogen until
385 data collection.

386

387 ***Data collection***

388 Data were collected at LonCEM (The Frances Crick Institute, London, UK) at 300 kV on a Titan
389 Krios electron microscope (Thermo Fisher Scientific, Waltham, MA USA), equipped with a
390 Gatan K3 detector operating in counted super-resolution mode. Movies were acquired using
391 EPU (Thermo Fisher Scientific). Data were collected from four grids across separate sessions,
392 without hardware binning at a calibrated pixel size of 0.55 Å. Target defocus was -1 to -3.5
393 μm, with a total dose of 50 electrons per $Å^2$, during an exposure time of 3.9 to 5 seconds,
394 fractionated into 38-50 frames.

395

396 ***Data processing***

397 An overview of the workflow used to process data is provided in **Fig. S1**. In summary, all movie
398 frames were aligned using 5 x 5 patches in Motioncor2 with dose-weighting (Zheng et al.
399 2017). All data were binned by a factor of 2. Contrast transfer function (CTF) parameters were
400 estimated using CTFFIND4 (Rohou and Grigorieff 2015). Particles were picked using Topaz
401 (Bepler et al. 2019) integrated into CryoSPARC. Initial training used a set of particles manually
402 picked from a few micrographs, with the resultant 'trained' model being used to auto-pick
403 particles across all micrographs. Apart from the 'Head-only' approach, all processing was
404 carried out in parallel, using both CryoSPARC (v3.1.0, Punjani et al. 2017) and RELION (v3.1,
405 (Zivanov et al. 2018)) software suites to yield similar set of maps. For the sake of simplicity
406 and brevity, only the maps with the highest resolution estimates are reported here. All
407 refinements were performed using independent data half-sets (gold-standard refinement)
408 and resolutions determined based on the Fourier shell correlation (FSC = 0.143) criterion
409 (Rosenthal and Henderson 2003).

410

411 ***Holo-complex***

412 After several rounds of 2D classification in cryoSPARC, particles from 'good' classes were used
413 for an initial *ab initio* reconstruction. The resultant particles were exported to Relion and
414 then re-classified in 2D. Subsequent rounds of 3D classification in Relion yielded 6 classes, of
415 which one (1: HOLO-COMPLEXl; 17,152 particles, representing 13% of the input) provided the
416 highest resolution after 3D refinement with a soft-edged mask and solvent flattening. Post-
417 processing produced a map at 10.8 Å resolution.

418

419 ***Hinge/Arm and Head***

420 Working in parallel, using cryoSPARC, particle subtraction was used to remove the 'head-end'
421 of the complex, before additional rounds of 3D classification, refinement and post-processing
422 yielded a map at 8.53 Å (2: HINGE/ARM; 106,660 particles, 62.4% of input). A similar strategy
423 was used to remove the 'hinge-end' of the complex, however further rounds of processing
424 was halted due to the superior results obtained via the 'head-only' approach described below.

425

426 ***Head-only***

427 A second trained 'picking model' was used to identify particles corresponding to just the
428 'head-end' of the complex. After several rounds of 2D classification, particles from 'good'
429 classes were used for an initial *ab initio* reconstruction. After iterative rounds of 3D
430 classification and refinement, one class was selected to take forward into non-uniform
431 refinement, after removal of density corresponding to the HALO-tag attached to the Nse4
432 subunit by particle subtraction (3: HEAD-ONLY; 84,810 particles, 51.7% of input). Post-
433 processing yielded a map at 6.5 Å resolution.

434

435 ***Composite Map and Model Building***

436 An initial pseudo-atomic model for the Smc5/6-complex was generated by fitting of Phyre2-
437 generated homology models (Kelley et al. 2015) into map segments using programs of either
438 the PHENIX software suite (Liebschner et al. 2019) or ChimeraX (Pettersen et al. 2021; Afonine
439 et al. 2018; Liebschner et al. 2019), with additional manual positioning in either Coot (Emsley
440 et al. 2010) or PyMOL (The PyMOL Molecular Graphics System, Version 2.3.2, Schrödinger
441 LLC). Phenix.combine_focused_maps was used to generate a composite map, using each of
442 the reported maps with the initial model as an alignment reference. The initial homology
443 models were subsequently replaced with those generated by AlphaFold upon their public
444 release. The fit of the overall model was optimised by real-space refinement in PHENIX
445 against the composite map.

446

447 ***Data availability***

448 The two maps used to generate the composite cryo-EM volume have been deposited in the
449 Electron Microscopy Data Bank (EMDB) with accession codes EMD-13893 (head-end of
450 complex) and EMD-13894 (hinge and arm-region). Real-space refined coordinates for the
451 Smc5/6 model have been deposited in the Protein Data Bank (PDB) with accession code PDB-
452 7QCD. The accompanying composite cryo-EM volume has been deposited with accession
453 code: EMD-13895.

454

455 **Experiments in yeast**

456 Yeast strains were generated using the following procedure. Synthetic DNA encoding the
457 genomic sequence for both WT and mutant versions of each gene were purchased as 'Strings

458 DNA Fragments' from GeneArt (Thermo Fisher Scientfic, UK). These were cloned into the
459 vector pAW8-natMX6 (Watson et al. 2008), at the PaeI / SalI restriction sites, through Gibson
460 assembly via short regions of homology included during synthesis. PCR was then used to
461 amplify the gene and associated nourseothricin resistance module for introduction into the
462 endogenous locus of diploid yeast cells, using lithium acetate transformation.
463
464 ***Yeast Strains***
465 Strains were generated from 3 individual haploid isolates, generated from tetrad dissections.
466

Strain #	**Genotype**	**Reference**
2655	*MATalpha [leu2-3 trp1-1 ura3-1 can1-100 ADE2 his3-11,15]; haploid isolate, derived from W303*	(Thomas and Rothstein 1989)
2747 diploid	*MATa/alpha [leu2-3 trp1-1 ura3-1 can1-100 ade2-1/ADE2 his3-11,15 SMC5/smc5-Y961A, W964A]*	This study
2753 isolate 1	*MATa [leu2-3 trp1-1 ura3-1 can1-100 ADE2 his3-11,15 smc5-Y961A, W964A]*	This study
2755 isolate 2	*MATalpha [leu2-3 trp1-1 ura3-1 can1-100 ADE2 his3-11,15 smc5-Y961A, W964A]*	This study
2756 isolate 3	*MATalpha [leu2-3 trp1-1 ura3-1 can1-100 ADE2 his3-11,15 smc5-Y961A, W964A]*	This study
2745 diploid	*MATa/alpha [leu2-3 trp1-1 ura3-1 can1-100 ade2-1/ADE2 his3-11,15 SMC5/smc5-F972A, L978D, L981N]*	This study
2793 diploid	*MATa/alpha [leu2-3 trp1-1 ura3-1 can1-100 ade2-1/ADE2 his3-111,15 NSE1/nse1-F217A, E228R, R242A]*	This study

2794 isolate 1	*MATa [leu2-3 trp1-1 ura3-1 can1-100 ADE2 his3-111,15 nse1-F217A, E228R, R242A]*	This study
2795 isolate 2	*MATa [leu2-3 trp1-1 ura3-1 can1-100 ADE2 his3-111,15 nse1-F217A, E228R, R242A]*	This study
2796 isolate 3	*MATalpha [leu2-3 trp1-1 ura3-1 can1-100 ADE2 his3-111,15 nse1-F217A, E228R, R242A]*	This study

467

468 **Figures**

469 Molecular images were generated using either PyMOL (v. 2.3.2) or ChimeraX (v. 1.1.1).

470

ACKNOWLEDGEMENTS

The authors would like to thank Dr. Adam Watson, Dr. Alessandro Bianchi, Prof. Uli Rass, Prof. Antony Carr [AMC] and Prof. Laurence Pearl [LHP] (University of Sussex) for advice, discussion, and access to reagents/equipment. We are also grateful to the cryo-EM facility at the University of Sussex (funded by a Wellcome Trust award enhancement grant 095605/Z/11/A to LHP and the RM Phillips Trust). The work was supported by funding from: University of Sussex Strategic Development Fund [JB], Wellcome [110047/Z/15/Z; AMC], Cancer Research UK [C302/A24386; AWO and LHP] and MRC [MR/PO18955/1; JMM and AWO]. Funding for open access charge: Medical Research Council, University of Sussex Open Access Team (Library).

Conflict of interest statement: None declared.

FIGURE 1

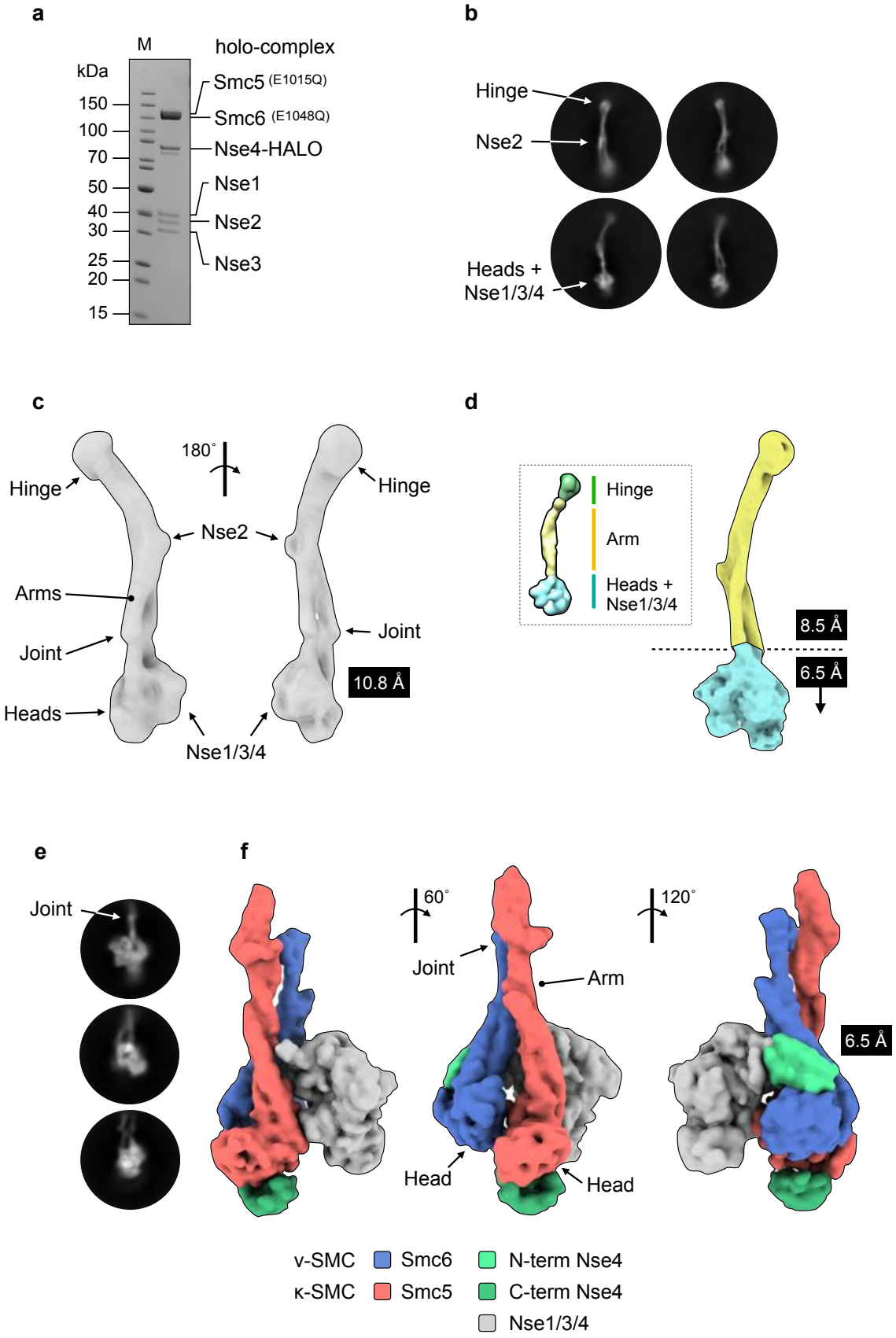
a
M
holo-complex
kDa
150
100
70
50
40
30
25
20
15
Smc5 (E1015Q)
Smc6 (E1048Q)
Nse4-HALO
Nse1
Nse2
Nse3
b
Hinge
Nse2
Heads +
Nse1/3/4
c
180˚
Hinge
Hinge
Nse2
Arms
Joint
Joint
Heads
10.8 Å
Nse1/3/4
d
Hinge
Arm
Heads +
Nse1/3/4
8.5 Å
6.5 Å
e
Joint
f
60˚
120˚
Joint
Arm
Head
Head
6.5 Å
ν-SMC
κ-SMC
Smc6
Smc5
N-term Nse4
C-term Nse4
Nse1/3/4

483 **Fig. 1. Cryo-EM of the budding yeast Smc5/6 complex**

484 (a) Representative SDS-PAGE gel for the purified Smc5/6 holo-complex. (b) Representative 2D
485 class averages (side views). Conformational flexibility leads to blurring of density at either the
486 head (top) or hinge-end (bottom) of the complex. (c) Initial 3D map from cryo-EM at a
487 resolution of 10.8 Å. (d) Maps from focussed refinement at 8.5Å and 6.5 Å for the indicated
488 segments of the Smc5/6 holo-complex (d, inset) model obtained by uranyl acetate negative
489 stain electron microscopy for comparison (Hallett et al. 2021). (e) Representative 2D class
490 averages (side views) and (f) resultant 3D map at 6.5 Å for the 'head'-end of the complex. The
491 cryo-EM map has been segmented and coloured with respect to its assigned component (see
492 associated key for additional detail).

FIGURE 2

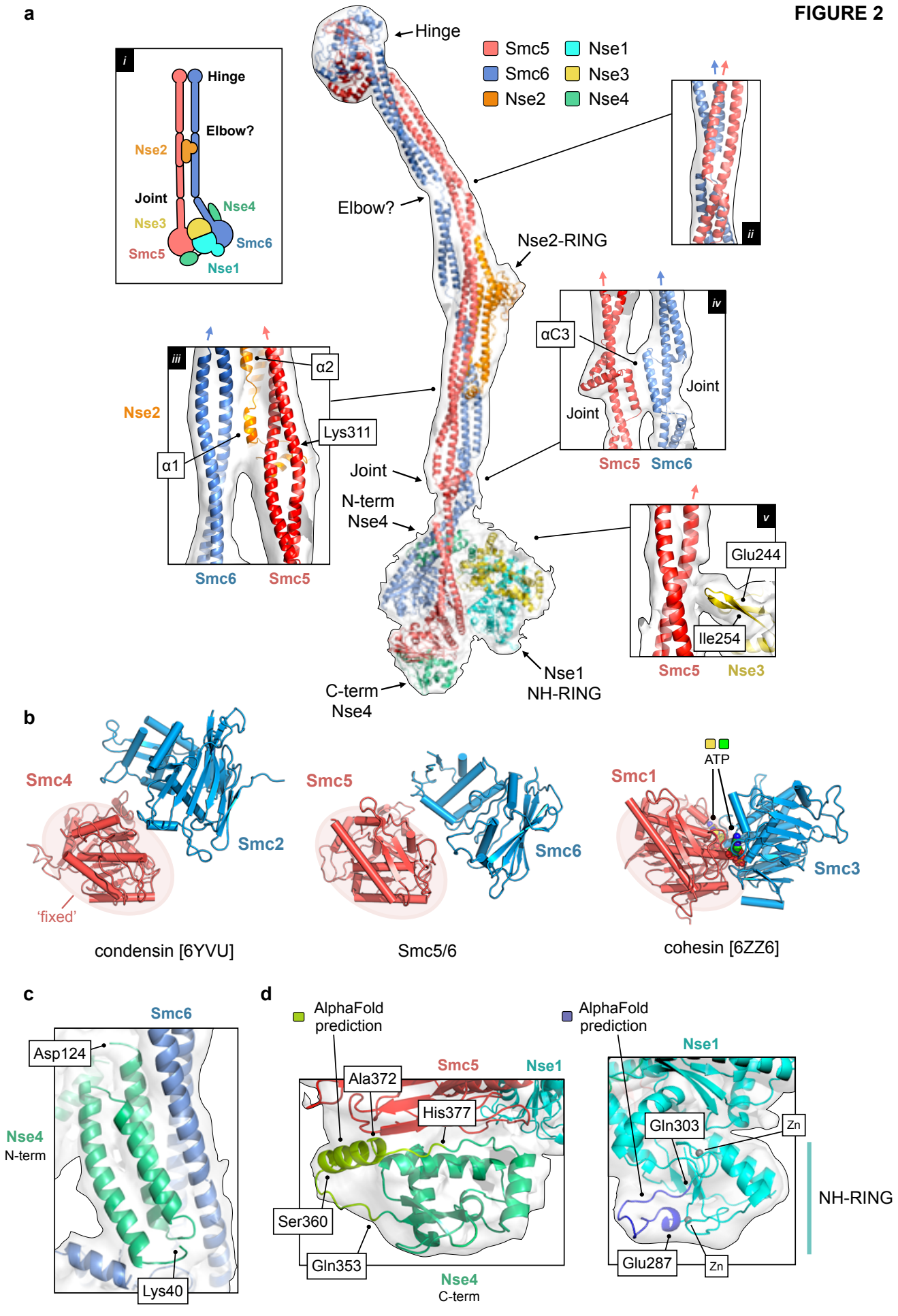
a
Hinge
Smc5
Smc6
Nse2
Nse1
Nse3
Nse4
i
Hinge
Elbow?
Nse2
Joint
Nse4
Nse3
Smc6
Smc5
Nse1
Elbow?
Nse2-RING
ii
iii
α2
Nse2
Lys311
α1
Smc6
Smc5
Joint
N-term
Nse4
iv
αC3
Joint
Joint
Smc5
Smc6
v
Glu244
Ile254
Smc5
Nse3
C-term
Nse4
Nse1
NH-RING
b
Smc4
Smc2
'fixed'
condensin [6YVU]
Smc5
Smc6
Smc5/6
Smc1
ATP
Smc3
cohesin [6ZZ6]
c
Smc6
Asp124
Nse4
N-term
Lys40
d
AlphaFold
prediction
Ala372
Smc5
Nse1
His377
Ser360
Gln353
Nse4
C-term
AlphaFold
prediction
Nse1
Gln303
Zn
NH-RING
Glu287
Zn

493 **Fig. 2. A pseudo-atomic model for the Smc5/6 holo-complex**

494 (a) Overview of the pseudo-atomic model. (a, inset *i*) Schematic showing the overall
495 architecture of the Smc5/6 complex and selected molecular features. (a, inset *ii*) Expanded
496 view of the 'Elbow', highlighting the crossover of the coiled-coil 'arms' of Smc5 and Smc6 at
497 this point. (a, inset *iii*) The first alpha-helix of Nse2 (α1) is situated between the two arms of
498 the complex. The position of Lys311, a known site of auto-SUMOylation is also indicated (a,
499 inset *iv*) Expanded view of the interface between the 'Joint' features of Smc5 and Smc5,
500 involving the two αC3 helices. (a, inset *v*) A short beta-hairpin (amino acids Glu244-Ile254)
501 protruding from Nse3 is in close proximity to the arm of Smc5. For each inset, the
502 directionality of the ascending helix (head to hinge) is indicated by a blue or red arrow, for
503 Smc5 and Smc6 respectively. (b) Comparison of the relative head domain positions in the
504 cryo-EM structures of budding yeast condensin (PDB: 6YVU), Smc5/6 (this manuscript) and
505 cohesin (PDB: 6ZZ6); in each, using the head of the κ-SMC as a fixed reference point.
506 (c) Expanded view for the N-terminal helical domain of Nse4 (aa Lys40-Asp124) bound to the
507 'arm' of Smc6. (d, left) AlphaFold predicts the presence of an additional helical element (aa
508 Ser360-Ala372) in the C-terminal domain of Nse4. (d, right). AlphaFold predicts a budding
509 yeast-specific loop insertion in the NH-RING of Nse1 (aa Glu287-Gln303). Where shown,
510 sections of density from the composite cryo-EM map are represented by a semi-transparent
511 molecular surface, shaded in grey. Please also see associated key for additional detail.

FIGURE 3

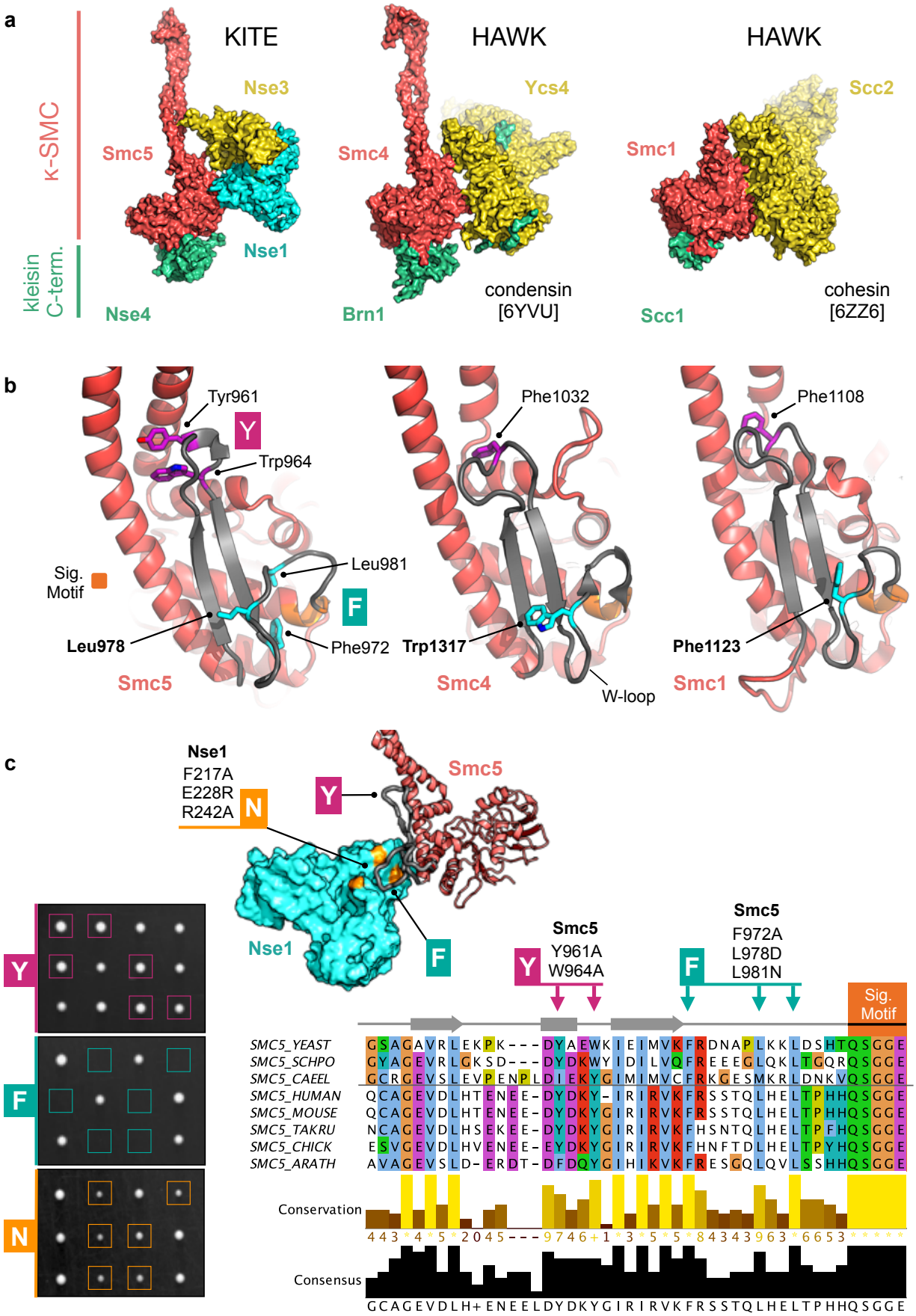
a
KITE
HAWK
HAWK
κ-SMC
kleisin C-term.
Nse3
Smc5
Nse1
Nse4
Ycs4
Smc4
Brn1
condensin [6YVU]
Scc2
Smc1
Scc1
cohesin [6ZZ6]
b
Tyr961
Y
Trp964
Sig. Motif
Leu981
F
Leu978
Phe972
Smc5
Phe1032
Trp1317
Smc4
W-loop
Phe1108
Phe1123
Smc1
c
Nse1
F217A
E228R
R242A
N
Y
Smc5
Nse1
F
Smc5
Y961A
W964A
Smc5
F972A
L978D
L981N
Sig. Motif
SMC5_YEAST
SMC5_SCHPO
SMC5_CAEEL
SMC5_HUMAN
SMC5_MOUSE
SMC5_TAKRU
SMC5_CHICK
SMC5_ARATH
Conservation
Consensus

512 **Fig. 3. KITES and HAWKS share a common interaction interface that involves the κ-SMC 'W-**
513 **loop'**
514 (a) Side-by-side visualisation of the κ-SMC head domain from Smc5/6 (left), condensin
515 (middle) and cohesin (right) in complex with their respective kleisin C-terminal domain; Nse4,
516 Brn1 and Scc1. In each case, the interacting partner, whether KITE or HAWK, makes a similar
517 set of interactions with the head domain of the κ-SMC. (b) Expanded view, showing
518 secondary structure molecular cartoons for each κ-SMC head domain, highlighting the
519 position of conserved amino acids within the 'W-loop' or equivalent (stick representation,
520 carbon atoms coloured cyan) plus aromatic residues within the preceding loop (stick
521 representation, carbon atoms coloured magenta). The ABC-signature motif is additionally
522 highlighted in orange. (c, left) Tetrad dissections. Spores derived from diploid *S. cerevisiae*
523 strains carrying both wild-type allele and indicated mutant allele plus associated NAT-
524 selectable marker (natMX6). Genotypes were confirmed by replica plating of spores on
525 selective media (not shown). (c, right) Multiple sequence alignment, across selected species,
526 showing conservation and consensus of amino acids within the W-loop and preceding region
527 of Smc5 (produced using Jalview 2 with Clustal X colour scheme; (Waterhouse et al. 2009)).
528 (c, top left) Relative positions of the Y and F mutation sets, with respect to the head domain
529 of Smc5 and Nse1 subunit (c, inset) Molecular secondary structure cartoon / surface
530 representation, showing the relative locations of the introduced mutation sets within the
531 Nse1/Smc5 interface. Sets of compound mutations introduced into budding yeast: Smc5-Y =
532 Y961A, W964A; Smc5-F = F972A, L978D, L981N, Nse1-N = F217A, E228R, R242A. Please also
533 see associated key for additional detail.

FIGURE 4

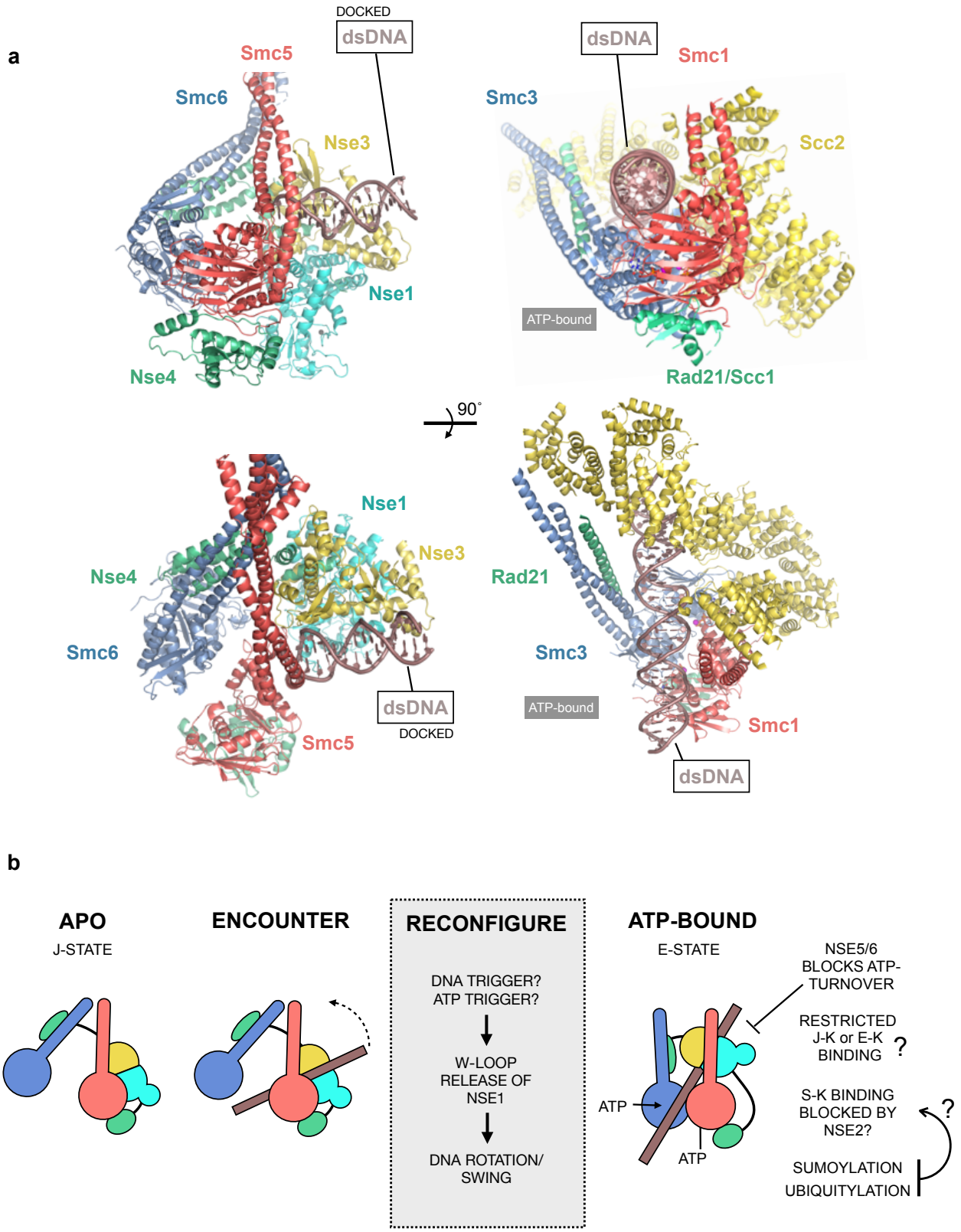
a
DOCKED
dsDNA
Smc5
Smc6
Nse3
Nse1
Nse4
dsDNA
Smc1
Smc3
Scc2
ATP-bound
Rad21/Scc1
90˚
Nse1
Nse3
Nse4
Smc6
dsDNA
DOCKED
Smc5
Rad21
Smc3
ATP-bound
Smc1
dsDNA
b
APO
J-STATE
ENCOUNTER
RECONFIGURE
DNA TRIGGER?
ATP TRIGGER?
W-LOOP
RELEASE OF
NSE1
DNA ROTATION/
SWING
ATP-BOUND
E-STATE
NSE5/6
BLOCKS ATP-
TURNOVER
RESTRICTED
J-K or E-K
BINDING
?
ATP
ATP
S-K BINDING
BLOCKED BY
NSE2?
?
SUMOYLATION
UBIQUITYLATION

534 **Fig. 4. A speculative model for dsDNA binding by the Smc5/6 complex**

535 (a) Secondary structure molecular cartoons comparing a docked pose for dsDNA-binding to
536 the Smc5/6 complex with cohesin in complex with ATP and dsDNA (PDB: 6ZZ6). The trajectory
537 of bound DNA was obtained by superposition of the docked pose reported in (Zabrady et al.
538 2016) for the human NSE1/3 hetero-dimer. (b) Model for conformational changes upon DNA
539 binding. We propose that transition from the apo, non-engaged state (J-state) to ATP-bound,
540 engaged (E-state) includes an intermediary 'encounter' complex — where dsDNA is first
541 bound to a positively charged surface/groove (created by the interface between Nse1 and
542 Nse3) — before a secondary reconfiguration step, triggered by either DNA or ATP-binding,
543 acts to release the Smc5 'W-loop' from its interaction with Nse1. This allows stimulation of
544 ATP turnover by the head domains and repositions the dsDNA such that it is bound with the
545 expected configuration (i.e., as in cohesin). It is not clear how, or indeed if, ubiquitylation,
546 SUMOylation or other post-translational modification affects either conformation or ATPase
547 activity. It is also not known if the presence of Nse2, acts to block binding or transition of
548 bound dsDNA into the S-K ring (SMC-kleisin) compartment, or if it serves to restrict it to the
549 J-K / E-K (juxtaposed-heads/kleisin or engaged head-kleisin) spaces. Binding of the Nse5/6
550 heterodimer blocks the ability of Smc5/6 to turn over ATP (Hallett et al. 2021; Taschner et al.
551 2021), but it is not known what effect this has on the overall conformation at the head-end
552 of the complex.

SUP. FIGURE 1

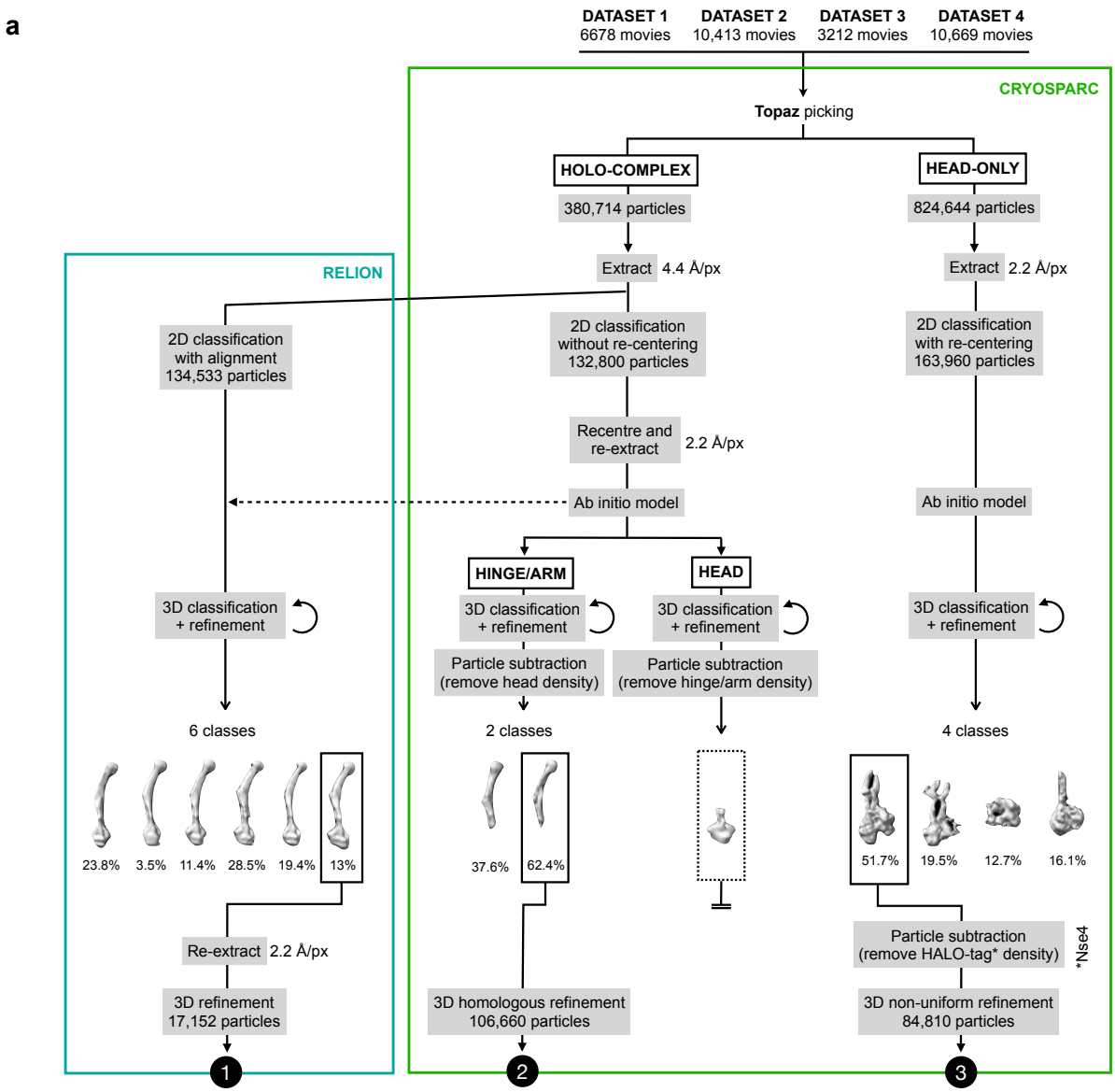
a
DATASET 1
6678 movies
DATASET 2
10,413 movies
DATASET 3
3212 movies
DATASET 4
10,669 movies
CRYOSPARC
Topaz picking
HOLO-COMPLEX
380,714 particles
Extract 4.4 Å/px
HEAD-ONLY
824,644 particles
Extract 2.2 Å/px
RELION
2D classification with alignment 134,533 particles
2D classification without re-centering 132,800 particles
2D classification with re-centering 163,960 particles
Recentre and re-extract 2.2 Å/px
Ab initio model
Ab initio model
HINGE/ARM
HEAD
3D classification + refinement
3D classification + refinement
3D classification + refinement
3D classification + refinement
Particle subtraction (remove head density)
Particle subtraction (remove hinge/arm density)
6 classes
2 classes
4 classes
23.8%
3.5%
11.4%
28.5%
19.4%
13%
37.6%
62.4%
51.7%
19.5%
12.7%
16.1%
Re-extract 2.2 Å/px
Particle subtraction (remove HALO-tag* density)
*Nse4
3D refinement 17,152 particles
3D homologous refinement 106,660 particles
3D non-uniform refinement 84,810 particles
1
2
3

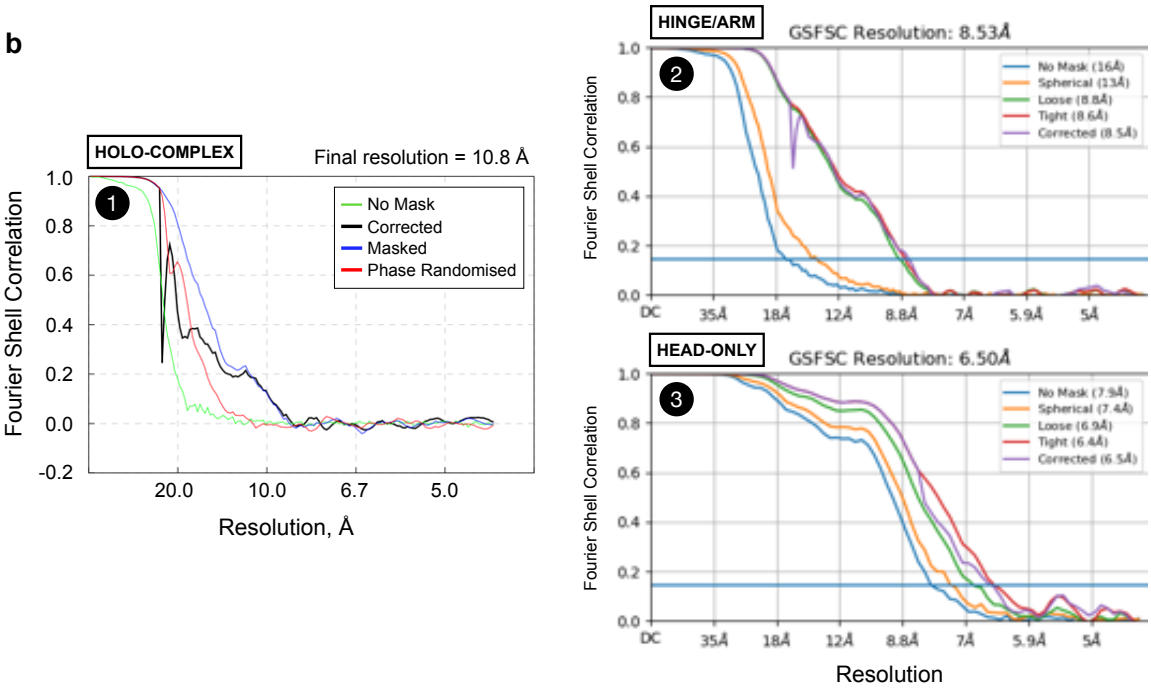
b
HOLO-COMPLEX
Final resolution = 10.8 Å
No Mask
Corrected
Masked
Phase Randomised
Fourier Shell Correlation
Resolution, Å
HINGE/ARM
GSFSC Resolution: 8.53Å
HEAD-ONLY
GSFSC Resolution: 6.50Å
Fourier Shell Correlation
Resolution

553 **Supplementary Figure 1**

554 (a) Summary of image-processing workflow, used to determine the structure of the budding
555 yeast Smc5/6 holo-complex. (b) Fourier Shell Correlation (FSC) curves estimating the average
556 resolution of the indicated maps.

SUP. FIGURE 2

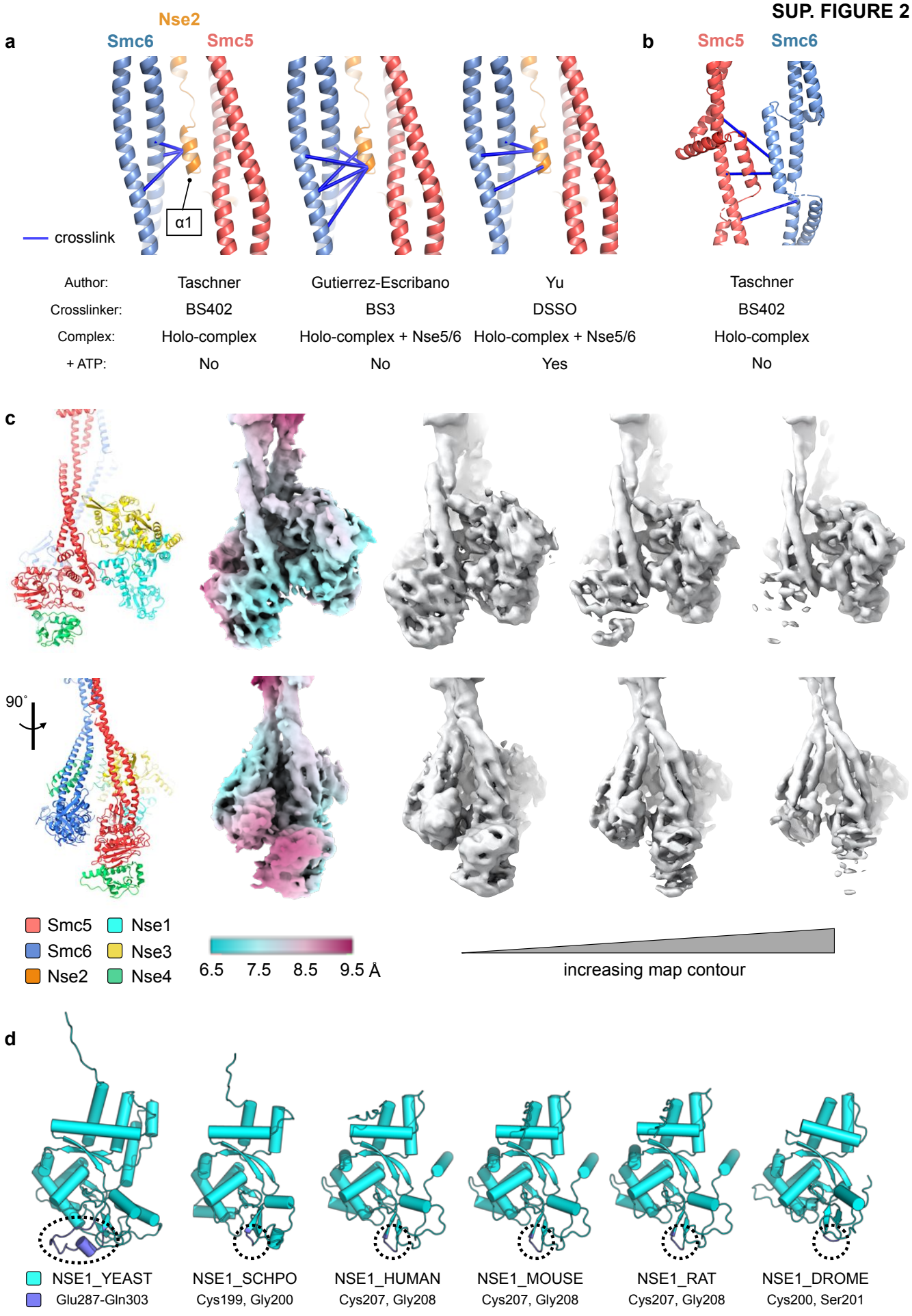
a
Nse2
Smc6
Smc5
α1
crosslink
b
Smc5
Smc6
Author:
Taschner
Gutierrez-Escribano
Yu
Taschner
Crosslinker:
BS402
BS3
DSSO
BS402
Complex:
Holo-complex
Holo-complex + Nse5/6
Holo-complex + Nse5/6
Holo-complex
+ ATP:
No
No
Yes
No
c
90°
Smc5
Smc6
Nse2
Nse1
Nse3
Nse4
6.5
7.5
8.5
9.5 Å
increasing map contour
d
NSE1_YEAST
Glu287-Gln303
NSE1_SCHPO
Cys199, Gly200
NSE1_HUMAN
Cys207, Gly208
NSE1_MOUSE
Cys207, Gly208
NSE1_RAT
Cys207, Gly208
NSE1_DROME
Cys200, Ser201

557 **Supplementary Figure 2**

558 (a) Selected cross-linking mass spectrometry (XL-MS) data taken from 3 separate studies,
559 supporting interaction of the first helix of Nse2 (α2) with the arm of Smc5. Study, type of
560 crosslinker used, complex composition and nucleotide status are summarised below the
561 molecular graphics. Cross-links were visualised using the PyXLinkViewer plugin (Serrano et al.
562 2020) for PyMOL (The PyMOL Molecular Graphics System, Version 2.3.2, Schrödinger, LLC).
563 XL-MS data reported in (Taschner et al. 2021), (Gutierrez-Escribano et al. 2020), (Yu et al.
564 2021). (b) Selected XL-MS data taken from (Taschner et al. 2021) supporting interaction of
565 the two SMC 'joints' in the Smc5/6 holo-complex. (c) Different representations for the 'head-
566 end' of the Smc5/6 complex. Sequentially from left to right: secondary structure molecular
567 cartoon; estimate of local resolution as calculated by ResMap-1.1.4 (Kucukelbir, Sigworth, and
568 Tagare 2014) mapped onto the surface of the composite cryo-EM map; composite map shown
569 at increasing contour levels. See associated keys for additional details. (d) AlphaFold predicts
570 the presence of a budding yeast-specific loop insertion in Nse1 (amino acids 287-303,
571 coloured dark blue).

SUP. FIGURE 3

a

Smc5 Y Y961A W964A

Nse1 N F217A E228R R242A

(WT) W303
#1
#2
#3

24 hours / YP

48 hrs / 100 mM HU

48 hrs / 50 J UV

48 hrs / 40 µM CPT

48 hrs / 0.005% MMS

b

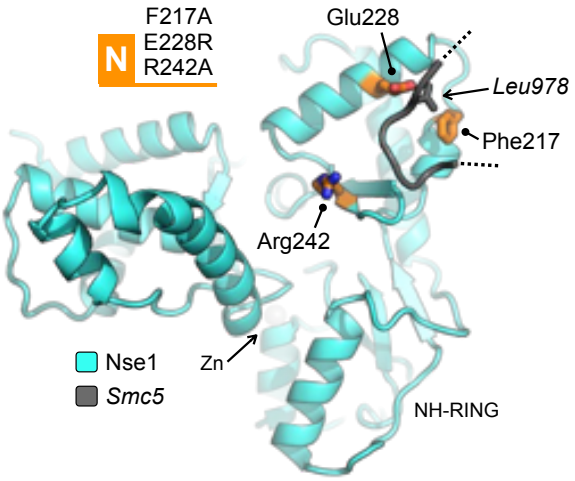

c

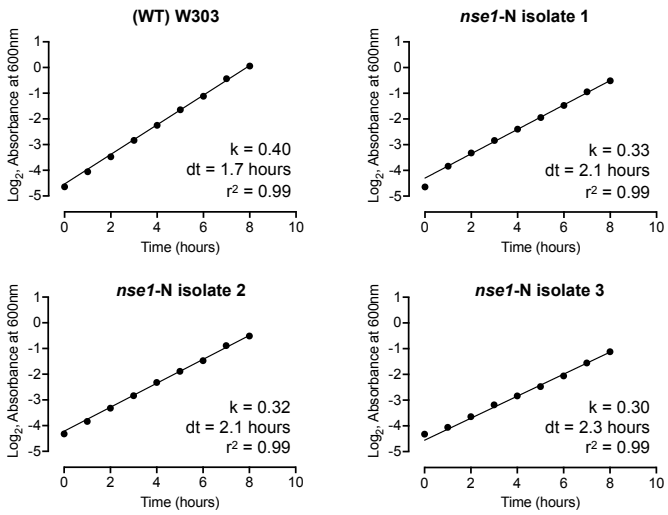

572 **Supplementary Figure 3**

573 (a) Yeast strains carrying the Y-set of Smc5 mutations are not sensitive to a range of genotoxic
574 agents and have no obvious growth defect. Those carrying the N-set of Nse1 mutations are
575 mildly sensitive to treatment with camptothecin (CPT) or methyl methanesulphonate (MMS).
576 Dose, type of treatment and duration of growth are as indicated; where HU = hydroxyurea,
577 UV = ultraviolet light. The W303 strain is included as a wild-type (WT) control. (b) Molecular
578 secondary structure cartoon highlighting the position of the mutated amino acid residues in
579 Nse1 (carbon atoms coloured in orange and shown in 'stick' representation) relative to that
580 of the Smc5 'W-loop' (coloured in dark grey, with the side chain of Leu978 shown in 'stick'
581 representation). Please also see associated key for additional details. (c) Representative
582 growth curves for the 3 isolates containing the N-set of mutations introduced into Nse1. The
583 W303 strain is included as a wild-type (WT) control. Data are fitted to an Exponential
584 (Malthusian) grown curve, with k defining a rate constant (slope), dt indicating the calculated
585 doubling time, and r^2 a goodness of fit parameter.

586

587 **REFERENCES**

588 Afonine, P. V., B. K. Poon, R. J. Read, O. V. Sobolev, T. C. Terwilliger, A. Urzhumtsev, and P. D.
589 Adams. 2018. 'Real-space refinement in PHENIX for cryo-EM and crystallography',
590 *Acta Crystallogr D Struct Biol*, 74: 531-44.
591 Alt, A., H. Q. Dang, O. S. Wells, L. M. Polo, M. A. Smith, G. A. McGregor, T. Welte, A. R.
592 Lehmann, L. H. Pearl, J. M. Murray, and A. W. Oliver. 2017. 'Specialized interfaces of
593 Smc5/6 control hinge stability and DNA association', *Nat Commun*, 8: 14011.
594 Anderson, D. E., A. Losada, H. P. Erickson, and T. Hirano. 2002. 'Condensin and cohesin display
595 different arm conformations with characteristic hinge angles', *J Cell Biol*, 156: 419-24.
596 Bentley, P., M. J. A. Tan, A. A. McBride, E. A. White, and P. M. Howley. 2018. 'The SMC5/6
597 Complex Interacts with the Papillomavirus E2 Protein and Influences Maintenance of
598 Viral Episomal DNA', *J Virol*, 92.
599 Bepler, T., A. Morin, M. Rapp, J. Brasch, L. Shapiro, A. J. Noble, and B. Berger. 2019. 'Positive-
600 unlabeled convolutional neural networks for particle picking in cryo-electron
601 micrographs', *Nat Methods*, 16: 1153-60.
602 Bermudez-Lopez, M., M. T. Villoria, M. Esteras, A. Jarmuz, J. Torres-Rosell, A. Clemente-
603 Blanco, and L. Aragon. 2016. 'Sgs1's roles in DNA end resection, HJ dissolution, and
604 crossover suppression require a two-step SUMO regulation dependent on Smc5/6',
605 *Genes Dev*, 30: 1339-56.
606 Burmann, F., B. G. Lee, T. Than, L. Sinn, F. J. O'Reilly, S. Yatskevich, J. Rappsilber, B. Hu, K.
607 Nasmyth, and J. Lowe. 2019. 'A folded conformation of MukBEF and cohesin', *Nat*
608 *Struct Mol Biol*, 26: 227-36.
609 Burmann, F., H. C. Shin, J. Basquin, Y. M. Soh, V. Gimenez-Oya, Y. G. Kim, B. H. Oh, and S.
610 Gruber. 2013. 'An asymmetric SMC-kleisin bridge in prokaryotic condensin', *Nat Struct*
611 *Mol Biol*, 20: 371-9.
612 Collier, J. E., B. G. Lee, M. B. Roig, S. Yatskevich, N. J. Petela, J. Metson, M. Voulgaris, A.
613 Gonzalez Llamazares, J. Lowe, and K. A. Nasmyth. 2020. 'Transport of DNA within
614 cohesin involves clamping on top of engaged heads by Scc2 and entrapment within
615 the ring by Scc3', *Elife*, 9.
616 Cutts, E. E., and A. Vannini. 2020. 'Condensin complexes: understanding loop extrusion one
617 conformational change at a time', *Biochem Soc Trans*, 48: 2089-100.
618 Datta, S., L. Lecomte, and C. H. Haering. 2020. 'Structural insights into DNA loop extrusion by
619 SMC protein complexes', *Curr Opin Struct Biol*, 65: 102-09.
620 Diebold-Durand, M. L., H. Lee, L. B. Ruiz Avila, H. Noh, H. C. Shin, H. Im, F. P. Bock, F. Burmann,
621 A. Durand, A. Basfeld, S. Ham, J. Basquin, B. H. Oh, and S. Gruber. 2017. 'Structure of
622 Full-Length SMC and Rearrangements Required for Chromosome Organization', *Mol*
623 *Cell*, 67: 334-47 e5.
624 Duan, X., P. Sarangi, X. Liu, G. K. Rangi, X. Zhao, and H. Ye. 2009. 'Structural and functional
625 insights into the roles of the Mms21 subunit of the Smc5/6 complex', *Mol Cell*, 35:
626 657-68.
627 Emsley, P., B. Lohkamp, W. G. Scott, and K. Cowtan. 2010. 'Features and development of
628 Coot', *Acta Crystallogr D Biol Crystallogr*, 66: 486-501.
629 Etheridge, T. J., D. Villahermosa, E. Campillo-Funollet, A. D. Herbert, A. Irmisch, A. T. Watson,
630 H. Q. Dang, M. A. Osborne, A. W. Oliver, A. M. Carr, and J. M. Murray. 2021. 'Live-cell
631 single-molecule tracking highlights requirements for stable Smc5/6 chromatin
632 association in vivo', *Elife*, 10.

633 Fennell-Fezzie, R., S. D. Gradia, D. Akey, and J. M. Berger. 2005. 'The MukF subunit of
634 Escherichia coli condensin: architecture and functional relationship to kleisins', *EMBO*
635 *J*, 24: 1921-30.
636 Fousteri, M. I., and A. R. Lehmann. 2000. 'A novel SMC protein complex in
637 Schizosaccharomyces pombe contains the Rad18 DNA repair protein', *EMBO J*, 19:
638 1691-702.
639 Gibson, R. T., and E. J. Androphy. 2020. 'The SMC5/6 Complex Represses the Replicative
640 Program of High-Risk Human Papillomavirus Type 31', *Pathogens*, 9.
641 Gligoris, T. G., J. C. Scheinost, F. Burmann, N. Petela, K. L. Chan, P. Uluocak, F. Beckouet, S.
642 Gruber, K. Nasmyth, and J. Lowe. 2014. 'Closing the cohesin ring: structure and
643 function of its Smc3-kleisin interface', *Science*, 346: 963-7.
644 Gutierrez-Escribano, P., S. Hormeno, J. Madariaga-Marcos, R. Sole-Soler, F. J. O'Reilly, K.
645 Morris, C. Aicart-Ramos, R. Aramayo, A. Montoya, H. Kramer, J. Rappsilber, J. Torres-
646 Rosell, F. Moreno-Herrero, and L. Aragon. 2020. 'Purified Smc5/6 Complex Exhibits
647 DNA Substrate Recognition and Compaction', *Mol Cell*, 80: 1039-54 e6.
648 Haering, C. H., D. Schoffnegger, T. Nishino, W. Helmhart, K. Nasmyth, and J. Lowe. 2004.
649 'Structure and stability of cohesin's Smc1-kleisin interaction', *Mol Cell*, 15: 951-64.
650 Hallett, S. T., P. Schellenberger, L. Zhou, F. Beuron, E. Morris, J. M. Murray, and A. W. Oliver.
651 2021. 'Nse5/6 is a negative regulator of the ATPase activity of the Smc5/6 complex',
652 *Nucleic Acids Res*, 49: 4534-49.
653 Hassler, M., I. A. Shaltiel, and C. H. Haering. 2018. 'Towards a Unified Model of SMC Complex
654 Function', *Curr Biol*, 28: R1266-R81.
655 Hassler, M., I. A. Shaltiel, M. Kschonsak, B. Simon, F. Merkel, L. Tharichen, H. J. Bailey, J.
656 Macosek, S. Bravo, J. Metz, J. Hennig, and C. H. Haering. 2019. 'Structural Basis of an
657 Asymmetric Condensin ATPase Cycle', *Mol Cell*, 74: 1175-88 e9.
658 Higashi, T. L., P. Eickhoff, J. S. Sousa, J. Locke, A. Nans, H. R. Flynn, A. P. Snijders, G.
659 Papageorgiou, N. O'Reilly, Z. A. Chen, F. J. O'Reilly, J. Rappsilber, A. Costa, and F.
660 Uhlmann. 2020. 'A Structure-Based Mechanism for DNA Entry into the Cohesin Ring',
661 *Mol Cell*, 79: 917-33 e9.
662 Jo, A., S. Li, J. W. Shin, X. Zhao, and Y. Cho. 2021. 'Structure Basis for Shaping the Nse4 Protein
663 by the Nse1 and Nse3 Dimer within the Smc5/6 Complex', *J Mol Biol*, 433: 166910.
664 Jumper, J., R. Evans, A. Pritzel, T. Green, M. Figurnov, O. Ronneberger, K. Tunyasuvunakool,
665 R. Bates, A. Zidek, A. Potapenko, A. Bridgland, C. Meyer, S. A. A. Kohl, A. J. Ballard, A.
666 Cowie, B. Romera-Paredes, S. Nikolov, R. Jain, J. Adler, T. Back, S. Petersen, D. Reiman,
667 E. Clancy, M. Zielinski, M. Steinegger, M. Pacholska, T. Berghammer, S. Bodenstein, D.
668 Silver, O. Vinyals, A. W. Senior, K. Kavukcuoglu, P. Kohli, and D. Hassabis. 2021. 'Highly
669 accurate protein structure prediction with AlphaFold', *Nature*.
670 Kamada, K., M. Su'etsugu, H. Takada, M. Miyata, and T. Hirano. 2017. 'Overall Shapes of the
671 SMC-ScpAB Complex Are Determined by Balance between Constraint and Relaxation
672 of Its Structural Parts', *Structure*, 25: 603-16 e4.
673 Kashammer, L., J. H. Saathoff, K. Lammens, F. Gut, J. Bartho, A. Alt, B. Kessler, and K. P.
674 Hopfner. 2019. 'Mechanism of DNA End Sensing and Processing by the Mre11-Rad50
675 Complex', *Mol Cell*, 76: 382-94 e6.
676 Kelley, L. A., S. Mezulis, C. M. Yates, M. N. Wass, and M. J. Sternberg. 2015. 'The Phyre2 web
677 portal for protein modeling, prediction and analysis', *Nat Protoc*, 10: 845-58.

678 Kong, M., E. E. Cutts, D. Pan, F. Beuron, T. Kaliyappan, C. Xue, E. P. Morris, A. Musacchio, A.
679 Vannini, and E. C. Greene. 2020. 'Human Condensin I and II Drive Extensive ATP-
680 Dependent Compaction of Nucleosome-Bound DNA', *Mol Cell*, 79: 99-114 e9.
681 Kschonsak, M., F. Merkel, S. Bisht, J. Metz, V. Rybin, M. Hassler, and C. H. Haering. 2017.
682 'Structural Basis for a Safety-Belt Mechanism That Anchors Condensin to
683 Chromosomes', *Cell*, 171: 588-600 e24.
684 Kucukelbir, A., F. J. Sigworth, and H. D. Tagare. 2014. 'Quantifying the local resolution of cryo-
685 EM density maps', *Nat Methods*, 11: 63-5.
686 Kurokawa, Y., and Y. Murayama. 2020. 'DNA Binding by the Mis4(Scc2) Loader Promotes
687 Topological DNA Entrapment by the Cohesin Ring', *Cell Rep*, 33: 108357.
688 Lee, B. G., F. Merkel, M. Allegretti, M. Hassler, C. Cawood, L. Lecomte, F. J. O'Reilly, L. R. Sinn,
689 P. Gutierrez-Escribano, M. Kschonsak, S. Bravo, T. Nakane, J. Rappsilber, L. Aragon, M.
690 Beck, J. Lowe, and C. H. Haering. 2020. 'Cryo-EM structures of holo condensin reveal
691 a subunit flip-flop mechanism', *Nat Struct Mol Biol*, 27: 743-51.
692 Li, Y., K. W. Muir, M. W. Bowler, J. Metz, C. H. Haering, and D. Panne. 2018. 'Structural basis
693 for Scc3-dependent cohesin recruitment to chromatin', *Elife*, 7.
694 Liebschner, D., P. V. Afonine, M. L. Baker, G. Bunkoczi, V. B. Chen, T. I. Croll, B. Hintze, L. W.
695 Hung, S. Jain, A. J. McCoy, N. W. Moriarty, R. D. Oeffner, B. K. Poon, M. G. Prisant, R.
696 J. Read, J. S. Richardson, D. C. Richardson, M. D. Sammito, O. V. Sobolev, D. H.
697 Stockwell, T. C. Terwilliger, A. G. Urzhumtsev, L. L. Videau, C. J. Williams, and P. D.
698 Adams. 2019. 'Macromolecular structure determination using X-rays, neutrons and
699 electrons: recent developments in Phenix', *Acta Crystallogr D Struct Biol*, 75: 861-77.
700 Matityahu, A., and I. Onn. 2021. 'Hit the brakes - a new perspective on the loop extrusion
701 mechanism of cohesin and other SMC complexes', *J Cell Sci*, 134.
702 Murayama, Y., and F. Uhlmann. 2014. 'Biochemical reconstitution of topological DNA binding
703 by the cohesin ring', *Nature*, 505: 367-71.
704 Murphy, C. M., Y. Xu, F. Li, K. Nio, N. Reszka-Blanco, X. Li, Y. Wu, Y. Yu, Y. Xiong, and L. Su.
705 2016. 'Hepatitis B Virus X Protein Promotes Degradation of SMC5/6 to Enhance HBV
706 Replication', *Cell Rep*, 16: 2846-54.
707 Palecek, J. J. 2018. 'SMC5/6: Multifunctional Player in Replication', *Genes (Basel)*, 10.
708 Palecek, J. J., and S. Gruber. 2015. 'Kite Proteins: a Superfamily of SMC/Kleisin Partners
709 Conserved Across Bacteria, Archaea, and Eukaryotes', *Structure*, 23: 2183-90.
710 Payne, F., R. Colnaghi, N. Rocha, A. Seth, J. Harris, G. Carpenter, W. E. Bottomley, E. Wheeler,
711 S. Wong, V. Saudek, D. Savage, S. O'Rahilly, J. C. Carel, I. Barroso, M. O'Driscoll, and R.
712 Semple. 2014. 'Hypomorphism in human NSMCE2 linked to primordial dwarfism and
713 insulin resistance', *J Clin Invest*, 124: 4028-38.
714 Petela, N. J., T. G. Gligoris, J. Metson, B. G. Lee, M. Voulgaris, B. Hu, S. Kikuchi, C. Chapard, W.
715 Chen, E. Rajendra, M. Srinivisan, H. Yu, J. Lowe, and K. A. Nasmyth. 2018. 'Scc2 Is a
716 Potent Activator of Cohesin's ATPase that Promotes Loading by Binding Scc1 without
717 Pds5', *Mol Cell*, 70: 1134-48 e7.
718 Petela, N. J., A. Gonzalez Llamazares, S. Dixon, B. Hu, B. G. Lee, J. Metson, H. Seo, A. Ferrer-
719 Harding, M. Voulgaris, T. Gligoris, J. Collier, B. H. Oh, J. Lowe, and K. A. Nasmyth. 2021.
720 'Folding of cohesin's coiled coil is important for Scc2/4-induced association with
721 chromosomes', *Elife*, 10.
722 Pettersen, E. F., T. D. Goddard, C. C. Huang, E. C. Meng, G. S. Couch, T. I. Croll, J. H. Morris,
723 and T. E. Ferrin. 2021. 'UCSF ChimeraX: Structure visualization for researchers,
724 educators, and developers', *Protein Sci*, 30: 70-82.

725 Piazza, I., A. Rutkowska, A. Ori, M. Walczak, J. Metz, V. Pelechano, M. Beck, and C. H. Haering.
726 2014. 'Association of condensin with chromosomes depends on DNA binding by its
727 HEAT-repeat subunits', *Nat Struct Mol Biol*, 21: 560-8.
728 Pintilie, G., and W. Chiu. 2012. 'Comparison of Segger and other methods for segmentation
729 and rigid-body docking of molecular components in cryo-EM density maps',
730 *Biopolymers*, 97: 742-60.
731 Pintilie, G. D., J. Zhang, T. D. Goddard, W. Chiu, and D. C. Gossard. 2010. 'Quantitative analysis
732 of cryo-EM density map segmentation by watershed and scale-space filtering, and
733 fitting of structures by alignment to regions', *J Struct Biol*, 170: 427-38.
734 Rohou, A., and N. Grigorieff. 2015. 'CTFFIND4: Fast and accurate defocus estimation from
735 electron micrographs', *J Struct Biol*, 192: 216-21.
736 Rosenthal, P. B., and R. Henderson. 2003. 'Optimal determination of particle orientation,
737 absolute hand, and contrast loss in single-particle electron cryomicroscopy', *J Mol Biol*,
738 333: 721-45.
739 Serrano, D., G. Cordero, R. Kawamura, A. Sverzhinsky, M. Sarker, S. Roy, C. Malo, J. M. Pascal,
740 J. F. Marko, and D. D'Amours. 2020. 'The Smc5/6 Core Complex Is a Structure-Specific
741 DNA Binding and Compacting Machine', *Mol Cell*, 80: 1025-38 e5.
742 Shi, Z., H. Gao, X. C. Bai, and H. Yu. 2020. 'Cryo-EM structure of the human cohesin-NIPBL-
743 DNA complex', *Science*, 368: 1454-59.
744 Soh, Y. M., F. Burmann, H. C. Shin, T. Oda, K. S. Jin, C. P. Toseland, C. Kim, H. Lee, S. J. Kim, M.
745 S. Kong, M. L. Durand-Diebold, Y. G. Kim, H. M. Kim, N. K. Lee, M. Sato, B. H. Oh, and
746 S. Gruber. 2015. 'Molecular basis for SMC rod formation and its dissolution upon DNA
747 binding', *Mol Cell*, 57: 290-303.
748 Sole-Soler, R., and J. Torres-Rosell. 2020. 'Smc5/6, an atypical SMC complex with two RING-
749 type subunits', *Biochem Soc Trans*, 48: 2159-71.
750 Taschner, M., J. Basquin, B. Steigenberger, I. B. Schafer, Y. M. Soh, C. Basquin, E. Lorentzen,
751 M. Raschle, R. A. Scheltema, and S. Gruber. 2021. 'Nse5/6 inhibits the Smc5/6 ATPase
752 and modulates DNA substrate binding', *EMBO J*: e107807.
753 Thomas, B. J., and R. Rothstein. 1989. 'The genetic control of direct-repeat recombination in
754 Saccharomyces: the effect of rad52 and rad1 on mitotic recombination at GAL10, a
755 transcriptionally regulated gene', *Genetics*, 123: 725-38.
756 Uhlmann, F. 2016. 'SMC complexes: from DNA to chromosomes', *Nat Rev Mol Cell Biol*, 17:
757 399-412.
758 van der Crabben, S. N., M. P. Hennus, G. A. McGregor, D. I. Ritter, S. C. Nagamani, O. S. Wells,
759 M. Harakalova, I. K. Chinn, A. Alt, L. Vondrova, R. Hochstenbach, J. M. van Montfrans,
760 S. W. Terheggen-Lagro, S. van Lieshout, M. J. van Roosmalen, I. Renkens, K. Duran, I.
761 J. Nijman, W. P. Kloosterman, E. Hennekam, J. S. Orange, P. M. van Hasselt, D. A.
762 Wheeler, J. J. Palecek, A. R. Lehmann, A. W. Oliver, L. H. Pearl, S. E. Plon, J. M. Murray,
763 and G. van Haaften. 2016. 'Destabilized SMC5/6 complex leads to chromosome
764 breakage syndrome with severe lung disease', *J Clin Invest*, 126: 2881-92.
765 Varejao, N., E. Ibars, J. Lascorz, N. Colomina, J. Torres-Rosell, and D. Reverter. 2018. 'DNA
766 activates the Nse2/Mms21 SUMO E3 ligase in the Smc5/6 complex', *EMBO J*, 37.
767 Waterhouse, A. M., J. B. Procter, D. M. Martin, M. Clamp, and G. J. Barton. 2009. 'Jalview
768 Version 2--a multiple sequence alignment editor and analysis workbench',
769 *Bioinformatics*, 25: 1189-91.

770 Watson, A. T., V. Garcia, N. Bone, A. M. Carr, and J. Armstrong. 2008. 'Gene tagging and gene
771 replacement using recombinase-mediated cassette exchange in Schizosaccharomyces
772 pombe', *Gene*, 407: 63-74.
773 Wells, J. N., T. G. Gligoris, K. A. Nasmyth, and J. A. Marsh. 2017. 'Evolution of condensin and
774 cohesin complexes driven by replacement of Kite by Hawk proteins', *Curr Biol*, 27: R17-
775 R18.
776 Woo, J. S., J. H. Lim, H. C. Shin, M. K. Suh, B. Ku, K. H. Lee, K. Joo, H. Robinson, J. Lee, S. Y. Park,
777 N. C. Ha, and B. H. Oh. 2009. 'Structural studies of a bacterial condensin complex
778 reveal ATP-dependent disruption of intersubunit interactions', *Cell*, 136: 85-96.
779 Xu, W., C. Ma, Q. Zhang, R. Zhao, D. Hu, X. Zhang, J. Chen, F. Liu, K. Wu, Y. Liu, and J. Wu. 2018.
780 'PJA1 Coordinates with the SMC5/6 Complex To Restrict DNA Viruses and Episomal
781 Genes in an Interferon-Independent Manner', *J Virol*, 92.
782 Xue, X., K. Choi, J. N. Bonner, T. Chiba, Y. Kwon, Y. Xu, H. Sanchez, C. Wyman, H. Niu, X. Zhao,
783 and P. Sung. 2014. 'Restriction of replication fork regression activities by a conserved
784 SMC complex', *Mol Cell*, 56: 436-45.
785 Yatskevich, S., J. Rhodes, and K. Nasmyth. 2019. 'Organization of Chromosomal DNA by SMC
786 Complexes', *Annu Rev Genet*, 53: 445-82.
787 Yu, Y., S. Li, Z. Ser, T. Sanyal, K. Choi, B. Wan, H. Kuang, A. Sali, A. Kentsis, D. J. Patel, and X.
788 Zhao. 2021. 'Integrative analysis reveals unique structural and functional features of
789 the Smc5/6 complex', *Proc Natl Acad Sci U S A*, 118.
790 Zabrady, K., M. Adamus, L. Vondrova, C. Liao, H. Skoupilova, M. Novakova, L. Jurcisinova, A.
791 Alt, A. W. Oliver, A. R. Lehmann, and J. J. Palecek. 2016. 'Chromatin association of the
792 SMC5/6 complex is dependent on binding of its NSE3 subunit to DNA', *Nucleic Acids*
793 *Res*, 44: 1064-79.
794 Zapatka, M., I. Pocino-Merino, H. Heluani-Gahete, M. Bermudez-Lopez, M. Tarres, E. Ibars, R.
795 Sole-Soler, P. Gutierrez-Escribano, S. Apostolova, C. Casas, L. Aragon, R. Wellinger, N.
796 Colomina, and J. Torres-Rosell. 2019. 'Sumoylation of Smc5 Promotes Error-free
797 Bypass at Damaged Replication Forks', *Cell Rep*, 29: 3160-72 e4.
798 Zawadzka, K., P. Zawadzki, R. Baker, K. V. Rajasekar, F. Wagner, D. J. Sherratt, and L. K.
799 Arciszewska. 2018. 'MukB ATPases are regulated independently by the N- and C-
800 terminal domains of MukF kleisin', *Elife*, 7.
801 Zheng, S. Q., E. Palovcak, J. P. Armache, K. A. Verba, Y. Cheng, and D. A. Agard. 2017.
802 'MotionCor2: anisotropic correction of beam-induced motion for improved cryo-
803 electron microscopy', *Nat Methods*, 14: 331-32.
804 Zivanov, J., T. Nakane, B. O. Forsberg, D. Kimanius, W. J. Hagen, E. Lindahl, and S. H. Scheres.
805 2018. 'New tools for automated high-resolution cryo-EM structure determination in
806 RELION-3', *Elife*, 7.